



# Hybrid Reynolds-Averaged/Large-Eddy Simulation Methodology from Symbolic Regression: Formulation and Application

Jack Weatheritt\* and Richard D. Sandberg†

University of Melbourne, Parkville, Victoria 3010, Australia

DOI: 10.2514/1.J055378

A unified hybrid Reynolds-averaged Navier–Stokes/large-eddy simulation closure is presented that is built from data-driven methods. This is a novel way to construct such models that does not impose constraints. Direct numerical simulation data is filtered, and the ratio of resolved to unresolved energy is used to fit an ideal length scale damping function for the unified framework. This study shows the viability of using high-fidelity data, not just for a priori testing but for the complete creation of lower-fidelity methods. Alongside the physical model, a convection scheme is proposed that marries well to it. This numerical scheme ensures that the damped turbulence model is provided the appropriate ratio of stability to accuracy. Furthermore, an additional function guarantees that the large-eddy simulation mode is only active in vortical flow. This hybrid closure is then applied to two industrially relevant yet very different geometries for which reliable reference data exist. The periodic hills test case is characterized by a confined separation and reattachment, whereas the tandem cylinders exhibits massive separation with wake interference patterns. For the latter, aeroacoustic predictions are of paramount importance. On both geometries, two mesh levels are tested. This a posteriori validation program provides a stern test for the new closure. For both resolutions on both geometries, the new formulation performs extremely well. Each case is also predicted using an established closure, and comparison to this further illustrates the potential of the current framework.

## Nomenclature

$a_{ij}^x$	=	extra anisotropy tensor (dimensional)
$f$	=	length scale damping function
$k$	=	$0.5\phi_{ii}$ turbulent kinetic energy of a stress tensor $\phi_{ij}$
$k^{2d}$	=	two-dimensional turbulent kinetic energy; $0.5(\tau_{11} + \tau_{22})$
$\mathcal{L}$	=	true integral scale of the flow
$\ell_\eta$	=	Kolmogorov length scale
$\ell^{\text{hyb}}$	=	hybrid length scale
$\ell^{\text{rans}}$	=	integral length scale (as estimated by turbulence model)
$Re_\ell$	=	Reynolds number with respect to length $\ell$
$S_{ij}$	=	strain rate tensor
$u_{\text{rans}}$	=	characteristic velocity of the unresolved scales
$\tilde{u}_i$	=	effective-filtered velocity
$\Delta$	=	grid width
$\partial_{x_j}$	=	Einstein summation implied; $\partial/\partial x_j$
$\varepsilon$	=	dissipation rate
$\nu_t, \nu_{\text{sgs}}$	=	eddy and subgrid viscosities
$\tau_{ij}, \tau_{ij}^{\text{hyb}}, \tau_{ij}^{\text{rans}}, \tau_{ij}^{\text{res}}$	=	exact, hybrid, Reynolds-averaged Navier–Stokes, and resolved Reynolds stress tensors
$\tau$	=	turbulent timescale
$\Omega_{ij}$	=	rotation rate tensor
$\omega$	=	specific dissipation rate

## I. Introduction

**A**S A tool for engineering design, direct numerical simulation (DNS) is impracticable. There are only a few complex turbulent

flow configurations for which solving the full Navier–Stokes is tenable (for example, [1–3]). The computational cost of obtaining complete flow information will restrict DNS to the academic domain for the foreseeable future, where it is highly useful as a tool for physics or as a tool for reference [4–6]. Instead, one must model part or all of the turbulent spectrum, with each option a classical method in computational fluid dynamics.

The first is large-eddy simulation (LES) [7]. As the name suggests, an LES models the small-scale motions while still resolving the majority of the turbulent energy. Chapman [8] estimated that an LES of a flat-plate boundary layer (of length  $L_x$ ) required a total number of grid points proportional to the Reynolds number ( $N \sim Re_{L_x}^{9/5}$ ) with an exponent only marginally better than DNS. Note that the exponent was later revised by Choi and Moin [9] to be 13/7. Furthermore, for a well-resolved LES, ~80% of the turbulent kinetic energy must be resolved [10]. The rest is smaller than the grid width  $\Delta$ , and so must be modeled. Classical subgrid-scale (SGS) models are suitable only when the modeled scales are isotropic. When the SGS model contributes significantly more than 20%, which is often termed very large-eddy simulation (VLES) [11], this constraint is violated and the results deteriorate. Such strong dependence on and poor scaling with the Reynolds number still puts the majority of industrially relevant geometries out of reach for an LES, yet it remains a useful tool in academia.

The second traditional modeling strategy for reducing the cost of DNS is to solve the Reynolds-averaged Navier–Stokes (RANS) equations [12,13]. The averaging procedure removes all scales except the mean, and thus the entire turbulence spectrum is modeled. This drastically reduces the cost of turbulent flow prediction; yet, this sacrifices accuracy in many cases (e.g., [14,15]). Furthermore, some applications demand the calculation of unsteady data. This includes aeroacoustic predictions that require accurate pressure fluctuations, energy spectra calculations that involve the turbulent kinetic energy at each wavelength, and even just knowledge of the Strouhal number is impossible with steady RANS alone. Despite these shortcomings, due to its computational affordability, RANS is the mainstay turbulence prediction tool in industry [16].

To bridge this gap between LES and RANS, hybrid RANS/LES methods have appeared that aim to be cheaper turbulence-resolving approaches by leaning on a RANS model in some way. The original concept behind combining RANS modeling with LES resolution is to ease the near-wall grid requirements of the latter [17]. The paradigm is often stated as follows: “perform RANS where required and LES where possible” [18]. This is often understood, with respect to simple

Presented as Paper 2015-0312 at the 53rd AIAA Aerospace Sciences Meeting, Kissimmee, FL, 5–9 January 2015; received 20 May 2016; revision received 12 April 2017; accepted for publication 18 April 2017; published online 6 July 2017. Copyright © 2017 by the American Institute of Aeronautics and Astronautics, Inc. All rights reserved. All requests for copying and permission to reprint should be submitted to CCC at www.copyright.com; employ the ISSN 0001-1452 (print) or 1533-385X (online) to initiate your request. See also AIAA Rights and Permissions www.aiaa.org/randp.

\*Postdoctoral Researcher, Department of Mechanical Engineering.

†Professor, Department of Mechanical Engineering. Senior Member AIAA.

wall-bounded flows, as treating the boundary layer with RANS and switching to LES in the outer layer. However, in some applications, due to the problem size exceeding computational capacity, a well-resolved LES is not possible in the far field and a VLES or even an unsteady RANS (URANS) regime must be settled for.

The combination of the two is made possible via the structural similarity of the momentum equations [11]. Note that a formal derivation of hybrid RANS/LES closures is not possible because we do not yet have knowledge of the operator analogous to those used in the deduction of the RANS and LES equations. Consequently, hybrids must begin from either RANS or LES. For example, methods may start from either temporal [19] or spatial [20] filtering, or a linear combination of the two [21]. As information reduction from a RANS model, which often contains two transport equations for inertial scales [22–24], is conceptually easier than adding information to an LES strategy, which often only relates the SGS contribution algebraically to the resolved scales and  $\Delta$  (for example, [25]), it is less problematic, and therefore more common, to produce hybrid RANS/LES methodologies from the former. However, as there is no commonality of model choice among the RANS community, there are multiple starting points for constructing hybrid RANS/LES. This has yielded a multitude of methodologies throughout the literature [11,26,27], which can be broadly categorized into three genera.

The first and earliest was born from a necessity to reduce the cost of a LES, known commonly as wall-modeled LES (WMLES). The seminal work of Schumann [28] and Deardorff [29] related the wall shear stress to the velocity in the core, assuming a universal law of the wall. These laws made it possible to relax the near-wall grid requirements, and good results [28] showed the feasibility of WMLES. This concept developed into two-layer modeling, which was first proposed by Balaras and Benocci [30]. This uses a coarse-grid LES up to the wall but embeds a second finer grid, which only marginally increases the cost of computation, for solving the near-wall region with the boundary-layer equations.

The second, known as zonal or sometimes segregated hybrid RANS/LES [31–34], employs two distinct regions. The interface between the two zones is prescribed by the user; often, turbulent fluctuations must be generated as a boundary condition for the LES.

The third is unified modeling, which uses the same set of equations globally. A universal momentum equation is solved at every point, whereas only the turbulent quantities are coupled. This control of the RANS/LES switch can be achieved either by blending between classic turbulence and subgrid models [35] or by a single model and its contribution damped to mimic a subgrid closure [36]. In practice, this can be done by modifying the turbulent length scale [17,18,37], subgrid viscosity [38], and turbulent kinetic energy [39], or by adding [40] or modifying [41] model dissipation source terms. It is the responsibility of a unified model to lower the effective viscosity, easing the burden on the user and potentially making a unified model more readily applicable. The lowering of this effective viscosity can be achieved through explicit use of  $\Delta$  or with flow quantities alone. Fröhlich and von Terzi [11] classified the former as “LES,” whereas they classified the latter as “URANS.”

Numerical methods also play a large role in determining the model regime. A large amount of numerical dissipation is often sufficient to reactivate RANS in LES zones, whereas the converse statement is true and often more damaging. That is, on very fine meshes, without any numerical dissipation, it is often difficult to force a model to run in RANS mode. This is because the model is inherently local and can therefore only be entrusted with estimating scales on the order of  $\Delta$ . To truly revert to RANS, on fine grids, the model must contain nonlocal information about the state of the boundary layer. Processes have been phenomenologically detailed, such as model stress depletion [42], the artificial near-wall cycle [43–45], and the more severe grid induced separation [46]: all of which occur in attached boundary layers. Such difficulties have largely limited unified models to studies of massively separated flows, whereas ongoing efforts attempt to resolve these issues [26,42,47].

In this work, we outline a methodology for creating a unified model, detailing the resultant formulation and a complementary numerical convection scheme. The methodology of formulation is

data driven rather than based on theory. It is our opinion that theoretical formulations of hybrid RANS/LES require too many presumptions. Often these assume conditions that are highly unlikely in practical scenarios. Model formulation is done a priori, and then it can be inserted into a RANS model. Gopalan et al. [48] also used a priori tools in the testing of model components; however, in this work, the model emerges naturally from this analysis without former prescription. **We do symbolic regression, using an evolutionary algorithm [49], on a DNS dataset to build a constraint free tangible equation for damping the turbulent length scale.** This study shows the viability of using such high-fidelity data to drive model formulation. Ongoing studies have shown that the numerical method must play a large role in the rectification of the current issues with unified hybrid RANS/LES: in particular, that the scheme must fit with the physical aspects of the model. Consequently, we have developed a tailored convection scheme alongside our novel formulation.

This paper is structured as follows. Our hybrid RANS/LES methodology is presented in Sec. II. This begins with a look at the specifics of the unified framework in Sec. II.A before commenting on the length scale damping function (Sec. II.B) and the details of its symbolic regression (Sec. II.C). The RANS model used is then discussed (Sec. II.D), and the framework is completed by looking at the novel convection scheme (Sec. II.E). In Sec. III, the new formulation is applied first to the periodic hills (Sec. III.A) and second to the tandem cylinders (Sec. III.B). Each case is also simulated using delayed detached-eddy simulation (DDES) [42] as a further comparison. Finally, conclusions are made in Sec. IV.

## II. Model Formulation

### A. Hybrid RANS/LES Framework

The unified flow simulation methodology (FSM) philosophy of Speziale is adopted [18,50,51]. Speziale [18] postulated that a hybrid should revert to a RANS in the coarse-grid limit, revert to a DNS in the fine-grid limit, and not contain any explicit filtering or averaging.

The effective-filtered momentum and continuity equations for an incompressible fluid

$$\partial_t \tilde{u}_i + \tilde{u}_j \partial_{x_j} \tilde{u}_i = -\partial_{x_i} \tilde{p} + \nu \partial_{x_j} \partial_{x_j} \tilde{u}_i - \partial_{x_j} \tau_{ij}^{\text{hyb}} \quad (1)$$

$$\partial_{x_i} \tilde{u}_i = 0 \quad (2)$$

are solved. The effective-filter is  $\tilde{(\cdot)}$ , and  $\tau_{ij}^{\text{hyb}}$  is the model term that must pick up the subgrid scales caused by this cutoff. As  $\Delta$  becomes sufficiently small (say,  $\Delta \sim \ell_\eta$ , with  $\ell_\eta$  being the Kolmogorov length scale),  $\tau_{ij}^{\text{hyb}} \rightarrow 0$  and Eq. (1) reduces to the Navier–Stokes equations. To respect the coarse-grid limit,  $\Delta \sim \mathcal{L}$  (with  $\mathcal{L}$  being the true integral length scale of the flow) and  $\tau_{ij}^{\text{hyb}}$  is a modified RANS turbulence model so that  $\tau_{ij}^{\text{hyb}} \rightarrow \tau_{ij}^{\text{rans}}$ . In this case, the effective filter is governed strongly by the turbulent viscosity from the model. Away from these limits, the RANS model acts in subgrid mode and the formulation can be thought of as non-classical LES. If  $\Delta$  is sufficiently small, then the effective filter is governed by the grid spacing. However, for coarse meshes, the effective filter is a combination of this spatial filtering with the effect from the model. Thus, it is the philosophy of unified hybrid RANS/LES to operate as a DNS, RANS, or anywhere in between, depending on the local values of  $\Delta$  and relevant turbulent length scales.

Consider the RANS constitutive stress–strain relationship:

$$\tau_{ij}^{\text{rans}} = \frac{2}{3} k \delta_{ij} - 2\nu_t S_{ij} + a_{ij}^x \quad (3)$$

where  $k$  is the turbulent kinetic energy,  $\nu_t$  is the eddy viscosity, and  $S_{ij}$  is the mean strain rate. By setting the extra anisotropy  $a_{ij}^x$  to zero, one recovers the linear Boussinesq approximation. In general,  $a_{ij}^x$  is a nonlinear polynomial in the velocity gradient tensor. For more detail, see the work of Pope [52] or Speziale et al. [53].

Equation (3) can be coerced into a hybrid formulation by

$$\tau_{ij}^{\text{hyb}} = \frac{2}{3} k \delta_{ij} - 2\nu_{\text{sgs}} \tilde{S}_{ij} + f a_{ij}^x \quad (4)$$

where the subgrid viscosity is given as follows:

$$\nu_{\text{sgs}} = f \nu_t \sim f \cdot (u_{\text{rans}} \ell^{\text{rans}}) = u_{\text{rans}} \cdot (f \ell^{\text{rans}}) = u_{\text{rans}} \ell^{\text{hyb}} \quad (5)$$

where  $\ell^{\text{rans}}$  and  $u_{\text{rans}}$  are the model estimates of the integral length and velocity scales. The hybrid length scale characteristic of the largest unresolved motions is  $\ell^{\text{hyb}}$ . Note that, because  $k$  is now the turbulent kinetic energy of the unresolved scales, the quantities  $\ell^{\text{rans}}$  and  $u_{\text{rans}}$  are no longer accurate estimates of the true integral scales of the flow. A damping function that is responsible for reducing  $\ell^{\text{hyb}}$  to be characteristic of the smallest resolved eddies is  $f$ . This damped length scale is then provided through the relation of Eq. (5) to Eq. (1), which is implicitly responsible for  $u_{\text{rans}}$ . This reduced turbulent diffusion thus results in  $u_{\text{rans}}$  being characteristic of the smallest resolved eddies. Therefore,  $\nu_{\text{sgs}}$  is defined with characteristic scales. Clearly, in practice, Eq. (5) is not an exact relation, as we do not have access to the RANS total quantities when  $f < 1$ ; however, as demonstrated through the rich history of FSM, and unified approaches in general, it still gives acceptable results. We then use our data-driven framework in an attempt to compensate for the fact we cannot calculate  $\ell^{\text{hyb}}$  accurately.

By similar arguments, consider the dissipation rate  $\epsilon$  first in a RANS framework:

$$\epsilon_{\text{rans}} \sim \frac{u_{\text{rans}}^3}{\ell^{\text{rans}}} \quad (6)$$

Then, for the hybrid formulation,

$$\epsilon \sim \frac{u_{\text{rans}}^3}{f \ell^{\text{rans}}} = \frac{u_{\text{rans}}^3}{\ell^{\text{hyb}}} \quad (7)$$

Therefore, to formulate a unified hybrid model from RANS, one may simply define

$$\ell^{\text{hyb}} = f \ell^{\text{rans}} \quad (8)$$

in place of all instances of  $\ell^{\text{rans}}$  throughout a RANS closure. Note that this is a key difference between the detached-eddy simulation (DES) and FSM philosophies: the former only damps  $\ell^{\text{rans}}$  in the dissipation term. Finally, it should be commented that the dissipation away from  $f \approx 1$  is now no longer a physical dissipation but rather acts as model dissipation.

## B. Comments on the Damping Function

The damping function  $f$  is the crucial element for success because it controls how much the length scale in the model is adjusted. The length scale should be damped by the appropriate amount, to the level that the grid can locally and instantaneously support. This should be done in a robust manner, such that the burden on the user is eased.

Many unified hybrid formulations can be rewritten in a manner similar to that in Sec. II.A with the definition of  $f$  as the differentiator (for example, [17,18,37]). This is because a formal derivation of a unified model depends on the effective filter. This mixture of spatial grid filtering and model contribution provides an obstacle to a true analytical means of closure. The result is an observed variety of ad hoc unified frameworks within the literature. One must always begin such a formulation from assumptions, which do not hold for every situation.

There is compelling evidence from LES studies that, on an LES-style mesh, the damping function should take the form  $f = C \cdot \Delta / \ell^{\text{rans}}$ , such that  $\ell^{\text{hyb}} = C \cdot \Delta$ . However, even on such grids, there is debate over the value of  $C$  [54]. Therefore, hybrids, which operate on coarser meshes still, cannot expect  $C$  to be constant;

indeed, there is a range of values exhibited by existing methodologies linear in  $\Delta / \ell^{\text{rans}}$ .

It is obvious that  $\ell^{\text{hyb}} = C \cdot \Delta$  will not suffice for all flow scenarios; as stated in the coarse limit,  $\ell^{\text{hyb}}$  will have to act as a length scale to a RANS model. For example, consider that the DDES damping function away from solid boundaries is  $f = 0.65 \Delta / \ell^{\text{rans}}$ . If  $\Delta \approx \mathcal{L} \approx \ell^{\text{rans}}$ , then the resolution is only sufficient for the integral scale; however, as  $C_{\text{DES}} < 1$ ,  $f \approx 0.65 (\Delta / \ell^{\text{rans}}) \approx 0.65 < 1$ . Therefore, on ambiguous meshes, DES recovers the RANS regime too late and acts as a poorly calibrated RANS model. It should be noted that, in the original presentation of the methodology, the authors specify sensible applications and grids such that DES does indeed function in the way that its name suggests. However, the methodology is not always applied carefully, and it falls to model developers to produce more robust damping functions.

## C. Evolutionary Approach to Formulation

We assume that  $f$  is a function of the turbulent scales  $\ell_\eta$  and  $\ell^{\text{rans}}$ , as well as  $\Delta$ . This is intuitive; through this functional dependency,  $f$  can assess the local and instantaneous turbulence and decide if the grid resolution is sufficient. Apart from this functional dependence, we construct  $f$  without making further physical assumptions and build a constraint-free model with symbolic regression. This sophisticated approach to searching the space of all functions for the best model without imposing a particular form uses mathematical building blocks and arranges them into rich and complex expressions. This is opposed to conventional regression, which seeks only to optimize parameters.

For a regression analysis training data is required to fit candidate models. This is a set of expected values of  $f$  for given values of  $\Delta$ ,  $\ell^{\text{rans}}$  and  $\ell_\eta$ . The hybrid RANS/LES is mimicked by a coarse filtering of a DNS (FDNS) flowfield. The FDNS data are free from turbulence modeling assumptions and allow for repeated testing of model candidates without the need of expensive hybrid RANS/LES simulations. The FDNS does, however, introduce a numerical assumption: that the explicit and effective filters are closely related.

The scales that are removed by the filter represent the subgrid motions that should be modeled  $\tau_{ij}^{\text{hyb}}$ . Scales not removed by the filter are those that should be resolved. The filter applied [55] is a central second-order explicit stencil, found by a weighted average of values at the grid point in question and those immediately adjacent:

$$\langle \phi_i \rangle_f = \sum_{j=i-1}^{i+1} c_j \phi_j \quad (9)$$

The adjacent points  $\phi_j$  are expanded in a Taylor series:

$$\phi_j = \sum_{k=0}^2 (\Delta_j) \phi_i^{(k)}, \quad i-1 \leq j \leq i+1 \quad (10)$$

The weightings  $c_j$  are found by constraining the transfer function  $T(\Theta = \pi) = 0$ , where  $0 \leq \Theta \leq \pi$  is the non-dimensional wave number, and setting their sum to unity:

$$\sum_{j=i-1}^{i+1} c_j = 1 \quad (11)$$

This allows for a linear system to be solved to obtain the filter kernel at grid location  $i$ .

In general, the filter kernel is a function of  $\Delta(x, y, z)$ ; but, for the case of a uniform grid,  $T$  is plotted in Fig. 1a. The independent variables  $\ell_\eta = (\nu / \epsilon^3)^{0.25}$  and  $\ell^{\text{rans}} = k^{1.5} / \epsilon$  are calculated as would be estimated by a turbulence model.  $\Delta$  is related to  $T$ , assuming the test filter will remove wave numbers larger than  $\Theta_c$  where  $T(\Theta_c) = 0.5$ .

The ideal form of the contribution function describes the amount of resolved stress over total stress, as derived by Germano [56]:

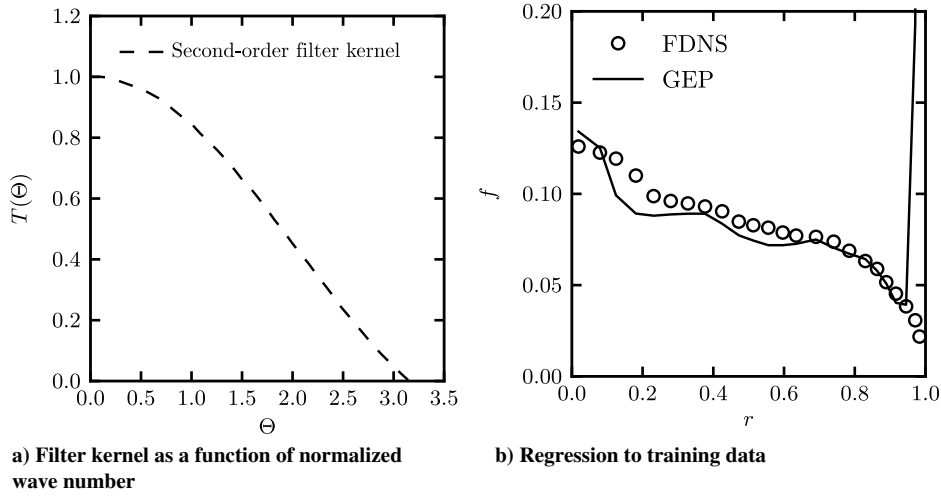


Fig. 1 Plots pertaining to the symbolic regression.

$$f^{\text{dns}} = 1 - \frac{\tau_{ij}^{\text{tot}} \tau_{ij}^{\text{res}}}{\tau_{mn}^{\text{tot}} \tau_{mn}^{\text{res}}} \quad (12)$$

where  $\tau_{ij}^{\text{res}} = \langle u_i u_j \rangle - \langle u_i \rangle \langle u_j \rangle$  is the time-averaged resolved stress, and  $\tau_{ij}^{\text{tot}}$  is the Reynolds stress from the unfiltered DNS. The required knowledge of  $\tau_{ij}^{\text{tot}}$  and the time average renders Eq. (12) impractical for actual simulations, as unsteady motions are not accounted for. Equation (12) can, however, be calculated for the FDNS data and serves as the dependent variable in the regression.

Figure 1b shows this function for well-resolved in-house DNS turbulent pipe data at  $Re_\tau = 3350$  based on radius  $r$ . Temporal averaging over 101 snapshots and spatial averaging across the homogeneous directions were used in the calculation of Eq. (12). The resulting dataset is used in this proof-of-concept study. Future work can expand on this significantly, both by varying the flowfield and the filtering operation.

To perform symbolic regression, the evolutionary framework known as gene expression programming (GEP) [49] is selected. An initial population of random functions, generated from the independent variables  $\Delta/\ell_\eta$  and  $\Delta/\ell_\eta^{\text{rans}}$ ; random constants; and the operators  $+$ ,  $-$ ,  $\times$ ,  $/$ ,  $\log$ ,  $\exp$ , and a power operator are evolved according to survival of the fittest:

$$\text{Fit}(f^{\text{guess}}) = 1 - \frac{1}{N} \sum_{k=1}^N \frac{|f_k^{\text{dns}} - f_k^{\text{guess}}|}{f_k^{\text{dns}}} \quad (13)$$

This measures how closely a candidate  $f^{\text{guess}}$  represents the FDNS data  $f^{\text{dns}}$  [calculated from Eq. (12)] for the  $N$  data points and should be maximized. Should a function be deemed “fit,” then it has a high probability of survival and reproducing (the mixing of two functions); otherwise, it is likely to die out. A further measure of fitness is added to control the simplicity of solutions. Functions that contain nested operators [i.e.,  $\exp(\exp(\exp(\sin(\dots))))$ ] are severely punished, and shorter functions are. This current evolutionary optimization is of the order of core minutes. Although this test case is relatively small, it shows the feasibility of more expansive future studies.

Figure 1b shows the results from the evolutionary process:

$$f^{\text{gep}} = c_1 \log \left( 1 + c_2 \frac{\Delta}{\ell_\eta} \right)^n \frac{\Delta}{\ell_\eta^{\text{rans}}} \quad (14)$$

where  $c_1$ ,  $c_2$ , and  $n$  are “random constants” [57] for which the value is free to change during the evolutionary process. These then must be calibrated for a given turbulence model and numerical code when implemented in practice (see the following). This calibration also serves to alleviate (to some extent) the implicit assumption of the filtering discussed previously.

The algorithm agrees with the general consensus, mentioned in Sec. II.B, that the damping function should be linear in  $\Delta/\ell_\eta^{\text{rans}}$ . However, the coefficient  $C = c_1 \log(1 + c_2 \Delta/\ell_\eta)^n$  is now damped by  $\ell_\eta$  as the DNS limit is approached, which allows for suitability on a wider range of meshes. Note that, in practice, this damping factor is bound by one to stop interference on coarser meshes. Our initial assumption of functional dependence on  $\ell_\eta^{\text{rans}}$ ,  $\ell_\eta$ , and  $\Delta$  is now justified with a good fit of the training data.

Equation (14) closely matches the FDNS contribution function with a discrepancy near the wall. This is because  $\ell_\eta^{\text{rans}} \rightarrow 0$  much faster than  $\Delta$  in this region. This is not an issue because Eq. (14) is inserted into Eq. (15), which controls the near-wall behavior in a manner similar to that of Weinmann et al. [51]:

$$f = \min \left( \frac{f^{\text{gep}}}{1 - f_b + 10^{-20}}, 1 \right) \quad (15)$$

The function  $f_b$  is defined in Eq. (32), which helps enforce  $f = 1$  in the boundary layer. Note that this equation is ad hoc and, as yet, it is not clear how the development of such a switching function can be incorporated into the regression framework.

Finally,  $c_i$  and  $n$  are calibrated for a channel flow of a friction Reynolds number of  $Re_\tau = 590$  [4] with  $N_y = 109$ . The RANS model for this calibration is discussed in Sec. II.D. The calibration matches  $\tau_{12}$  because, for industrially relevant applications, correctly predicting the shear stress is vital. The constants are found to be  $c_1 = 2.1$ ,  $c_2 = 0.75$ , and  $n = 4$ . Plots of the shear and normal stress are shown in Fig. 2a, whereas the velocity is plotted in Fig. 2b.

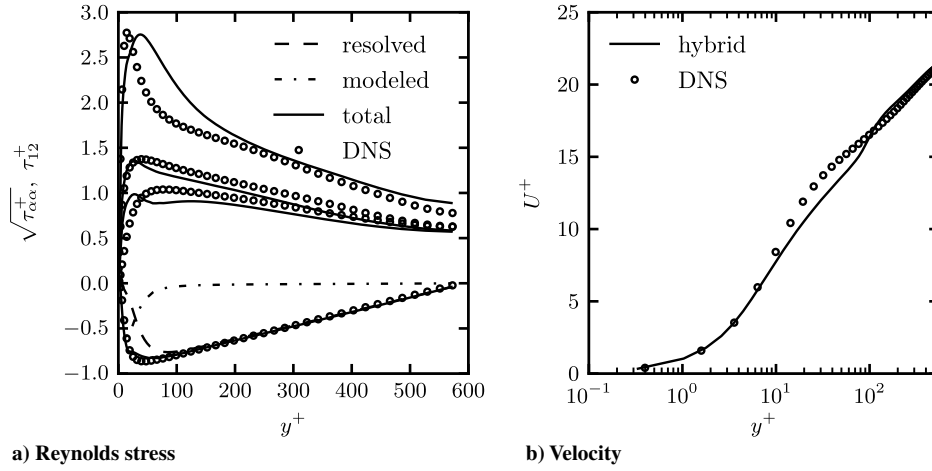
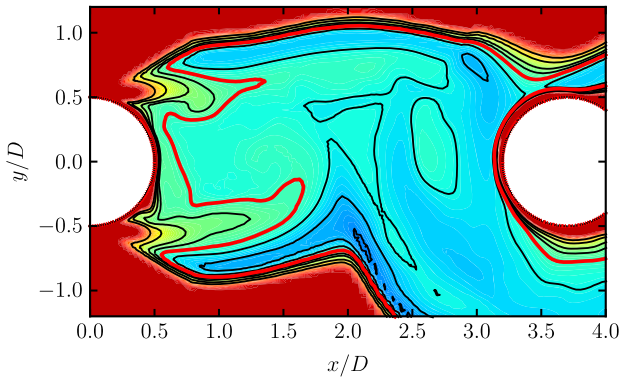
An instantaneous snapshot of the damping function is plotted in Fig. 3 for the tandem cylinder case described in Sec. III.B. The function is seen to adjust spatially with the flow, and the influence of the near-wall control preserves the RANS regime. A slight delay in the breaking down of the RANS shear layer can also be observed. Note the red contour line is discussed in Sec. II.E.

#### D. RANS Model Definition

The authors choose an explicit algebraic stress model (EASM) of a very similar form already used in hybrid RANS/LES [45,51] to close the equation set. The pressure-strain correlation of Speziale et al. [53] is the starting point for the turbulence model because it is derived for homogeneous turbulence and an assumption of slowly changing mean shear seems reasonable for the subgrid scales. For a detailed derivation of EASM-type models, see the work of Wallin and Johansen [58]. For a complete description of the particulars of the model, see the Appendix.

#### E. Numerical Considerations

The grid spacing  $\Delta$  is defined as the maximum dimension of each cell:

Fig. 2 Calibration for channel flow at  $Re_\tau = 590$ .Fig. 3 Instantaneous snapshot of  $f$ . Contour levels 0.3 to 1.0, red line:  $f = 0.5$ .

$$\Delta = \max(\Delta_x, \Delta_y, \Delta_z) \quad (16)$$

in accordance with sound advice regarding fine meshes [42]. This helps to alleviate the issue of model stress depletion for very fine streamwise grid spacing.

Unified hybrid RANS/LES requires special treatment of the convection term in Eq. (1). This is because RANS often requires stabilizing dissipation, whereas the unsteady regimes require a high-order-accurate scheme. A blending between upwinding and central differencing is used:

$$\sigma^{\text{hyb}} = \psi \sigma^{\text{up}} + (1 - \psi) \sigma^{\text{cds}} \quad (17)$$

via the use of a function  $\psi$  dependent on ratios of  $\Delta$  and turbulent length scale(s). The proposed scheme here uses the exact definition for  $f$  [Eq. (15)]. Whereas some authors [51,59] prefer to subtract a constant in the definition of  $\psi$ , by using Eq. (15), we provide a direct mapping between the model contribution level  $f$  and the required scheme blending  $\sigma^{\text{hyb}}$  that is bound for realizable values of  $f$ . In this work,  $f$  is defined:

$$\psi = \min \left[ 1, \frac{1}{1 - g + 10^{-20}} \max(1 - \exp^{-s_2 f^{s_3}}, s_1) \right] \quad (18)$$

Equation (18), plotted for  $g = 0$  in Fig. 4a, is bound between zero and one for DNS and RANS regimes, respectively. The constant  $s_1$  provides a baseline level of stabilizing upwind: in this work, set to zero. The constants  $s_2 = 12$  and  $s_3 = 10$  are used to shape the blending function after considering a range of mesh levels for a wide range of cases. Note that the values of these constants are appropriate for OpenFOAM, which is the flow solver used in the current work;

other codes may require significantly altered values. The shape of the function ensures that, in the URANS regime ( $f \approx 0.8$ ), upwinding is activated; whereas in the LES regime ( $f \approx 0.2$ ), central differencing is activated. In between, the constants provide a sharp initial drop in numerical dissipation as  $f \rightarrow 0$  before a slower transition to central differencing. This allows a quick switch to LES from RANS, yet it still provides a reasonable amount of stabilizing upwind in the VLES regime. Figure 4b demonstrates the consistency in prediction of the  $Re_\lambda = 730$  energy spectra [5] for two mesh levels. The base and fine meshes of  $32^3$  and  $64^3$  cells span the  $2\pi^3$  periodic box. For wave numbers resolved by the base mesh, there is no discernible difference between resolutions. Beyond the base mesh cutoff, the fine simulation potentially contains marginal artificial dissipation in the smallest resolved scales.

The function  $g$  is prepended to Eq. (18), in a fashion similar to Travin et al. [59], to ensure that the LES mode only becomes active in regions of strong vortical flow. Note that  $g$  is defined as

$$g = \frac{1}{2} - \frac{1}{2} \frac{\tilde{\Omega}^2 - \tilde{S}^2}{\tilde{\Omega}^2 + \tilde{S}^2} \quad (19)$$

where  $\tilde{S}^2$  and  $\tilde{\Omega}^2$  are the squared magnitude of the strain and rotation rate tensors. Equation (19) ensures also that  $f = 1$  near solid boundaries, even for very small values of  $\Delta_x$ , because it is based on flow and not mesh quantities.

Instantaneous values of  $g$  are plotted for the tandem cylinder case (Sec. III.B) in Fig. 5a, and its influence on  $\psi$  can be seen in Fig. 5b. This is the same snapshot as Fig. 3. The strong preservation of the RANS layer around the second cylinder can be observed in  $\psi$ . The red contour line ( $f = 0.5$ ) in Fig. 3 is the point in which central differencing becomes negligible if the function  $g$  is not active, which is already at the point of wake rollup. With  $g$  enabled, the switch to an LES is much quicker due to the vorticity of the resolved flowfield.

### III. Applications

The new formulation is applied to two contrasting flow problems. Furthermore, each case is performed at two mesh resolutions, testing the ability of the closure to adjust to coarse and fine grids. The first, which is the periodic hills case, is an internal flow; whereas the second, which is the tandem cylinders, is external. Both cases have a rich history of hybrid RANS/LES testing ([11,35,36,60–62] and [51,63–65], respectively). The periodic hills tests unsteady separation and reattachment forecasting by virtue of the closure alone. The tandem cylinders is a massively separated flow with the upstream wake disturbing the downstream shedding. Furthermore, there are aeroacoustic data available as comparison. These two test cases are therefore rigorous applications of the new model on relevant flow problems. Finally, we also calculate each case using the DDES implementation within OpenFOAM. These reference hybrid simulations are performed to illustrate our discussions in Sec. II.B.



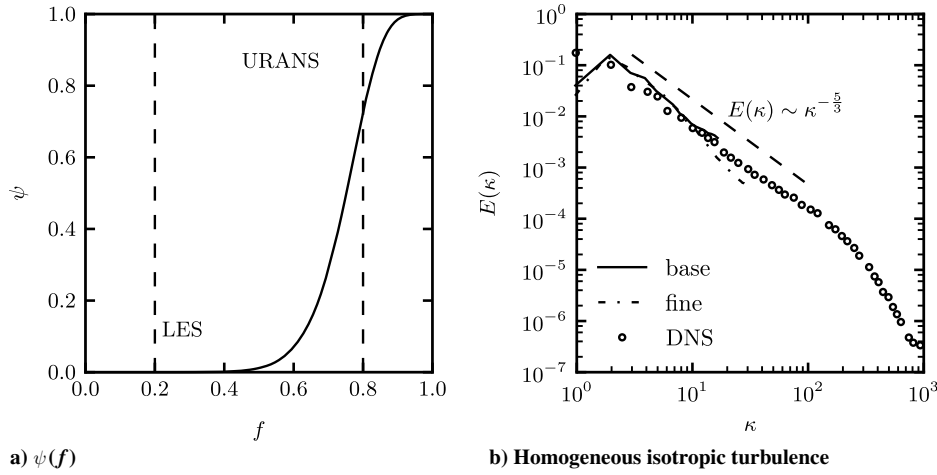


**Fig. 4** Numerical scheme as a function of damping function. Homogeneous isotropic turbulence energy spectra.

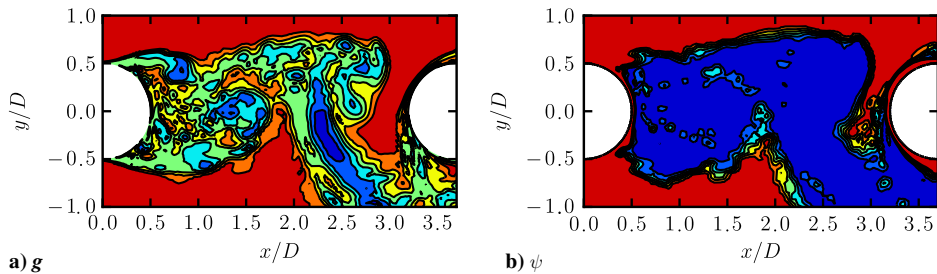


**Fig. 5** Numerical components. Contour levels are 0.1 increments from 0 to 1.

We use the recommended schemes for DDES, as it is beyond the scope of this paper to tailor numerics to a separate framework. This comparison therefore represents a same code model comparison to the state of the art available using our software of choice.

## A. Periodic Hills

### 1. Case Description

The flow over a series of continuously differentiable constrictions or “hills” in a two-dimensional channel produces an inherently unsteady point of separation. This produces additional large structures that propagate along the shear layer and reduce the reattachment length.

The hills, of height  $h$ , are separated crest to crest by  $L_x = 9h$  in a  $L_y = 3h$  tall channel of  $L_z = 4.5h$  spanwise extent. The Reynolds number based on the average velocity between the crest and the opposite wall is  $Re_h = 10,595$ . Periodic boundary conditions are applied in the streamwise and spanwise directions. The bulk velocity is maintained by enforcing a pressure gradient.

Two meshes are used in this study, and their parameters highlighted in Table 1. The baseline mesh, denoted as the base and consisting of 1.1 million cells ( $N_{\text{cells}}$ ), is almost double that of the coarse-mesh case, which is denoted as CM. Note that attention has been paid to ensure appropriate wall-normal resolution. Consequently, cells have been sacrificed in the spanwise direction and bulk region of the  $x$ - $y$  plane.

**Table 1** Mesh properties used for hybrid periodic hills cases<sup>a</sup>

	$N_{\text{cells}}$	$N_x$	$N_y$	$N_z$	$\bar{y}_1^+$ (top)	$\bar{y}_1^+$ (bottom)
Base	$1.1 \times 10^6$	138	130	60	<0.8	0.4 (1.27)
CM	600k	122	116	45	<0.8	0.5 (1.35)

<sup>a</sup> $\bar{y}_1^+$  in the brackets corresponds to the peak in skin-friction location before the crest of the hill; see Fig. 6e.

Highly resolved LES data [66], denoted as LES-Temmerman-Leschziner (LES-TL), are used as reference. The base mesh used here is one-quarter the size of this LES study, whereas the coarse mesh is one-eighth. Statistics are gathered by time averaging over  $1400U_b/h$  and  $1200U_b/h$  time units for the base and CM cases, respectively. Further averaging across the homogeneous span is performed.

### 2. Results

Figure 6 is a plot of vertical profiles of the first- and second-order statistics. Note that  $\tau_{ij}$  refers to the full Reynolds stress comprising both the resolved and modeled fluctuations, except the DDES that contains only the resolved contribution. Also included is the skin-friction coefficient along the lower surface. For the base and CM, our hybrid framework gives indistinguishable predictions for streamwise velocity (Fig. 6a) and shows only minor deviations for the second-order statistics (Figs. 6b–6d). Even the wall shear stress (Figs. 6e), which is a function of the boundary-layer shape and both resolved and modeled shear stress, shows a similar quality for both the base and CM cases. Note that the pure RANS model completely fails to predict the global flow features; reattachment is predicted at the base of the upstream side of the hill [45]. In general, the agreement is excellent with the reference LES-TL, and it is comparable to a previous DES study [62]. However, the DDES comparison presented has returned less than adequate results. This surprise appears to be a consequence of late separation, which is seen most clearly in Fig. 6e, that has been caused by a large overprediction of shear and wall-normal stress (Figs. 6b and 6d). This has altered the angle of the free shear layer; consequently, the early reattachment is reflected further in the velocity profiles. Note that the near-wall resolution is similar for both meshes, yielding a qualitatively similar flowfield; the coarsening in the shear layer has not altered the flowfield significantly. We acknowledge that other simulations with other meshes, numerical schemes, and codes provide good agreement using DDES [62,67]. The purpose of this comparison is not to highlight the inaccuracy of the DDES method for this case; rather, the

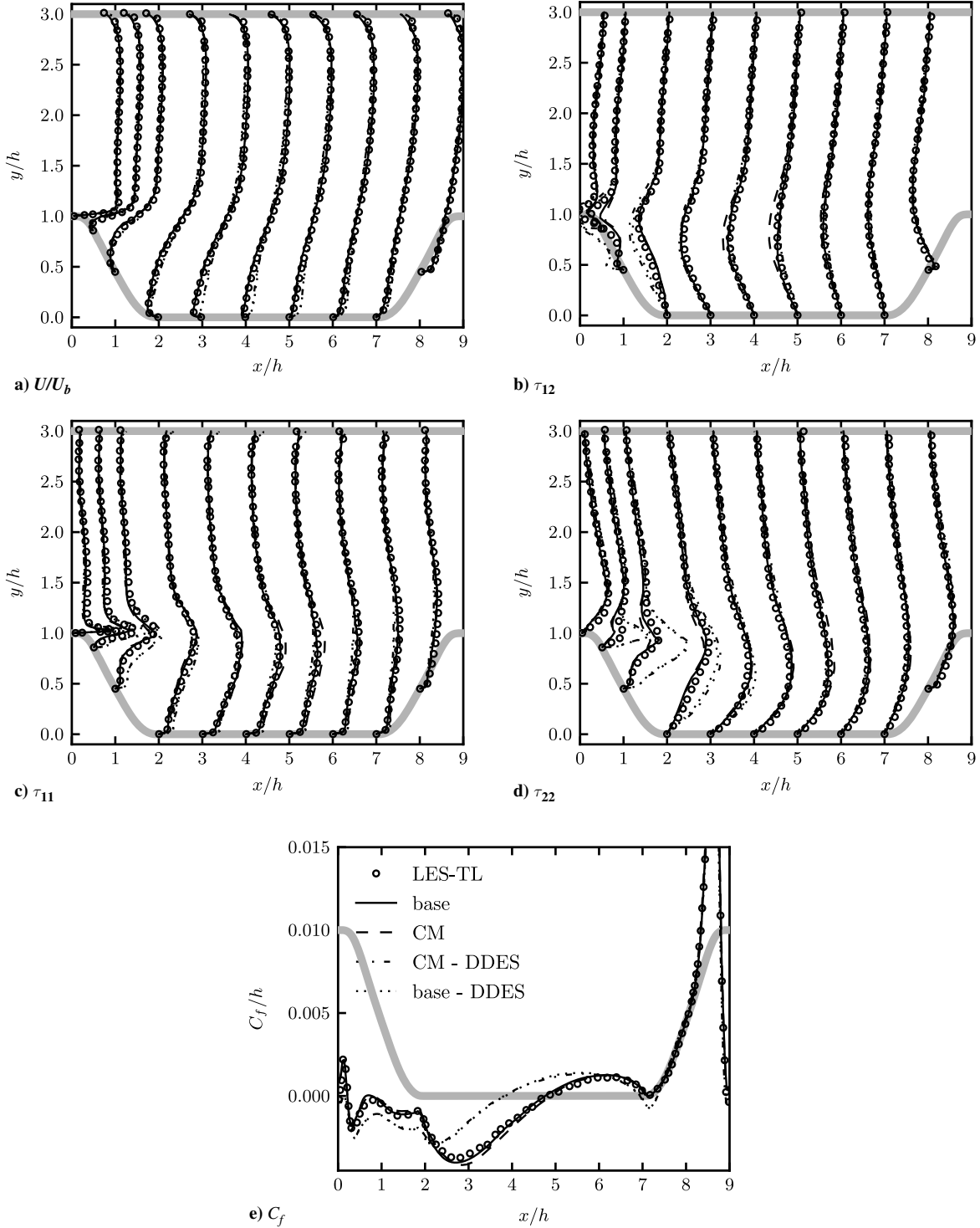


Fig. 6 Profiles of first and second order statistics for the periodic hills case.

implication is a high sensitivity of the DDES method using the recommended settings in OpenFOAM for this given mesh.

For our hybrid method, there is a slight lag, which is most noticeable in the CM case, in the formation of the shear-layer postseparation. Figures 6b–6d display the delayed breakdown of the separated RANS boundary layer, which subsequently develops too far downstream. Furthermore, a smearing of the shear layer at the point of impingement is observed. In reality, this is a mean phenomenon and the implication is that the delayed formation of structures coupled with the fluctuation of the separation point along the curved surface produces more variability in the angle of the free shear layer. This overprediction of shear stress is then modulated by the presence of the flow-facing side of the next hill.

## B. Tandem Cylinders

### 1. Case Description

Two cylinders of diameter  $D$ , with one  $3.7D$  downstream the other, are subject to a  $Re_D = 1.66 \times 10^5$  flow. The so-called tandem or inline cylinders case, which contains an abundance of rich experimental reference data [68–72], is challenging for numerical methodologies. Figure 7 is a schematic of the flowfield that exhibits a range of features that must be correctly captured. The point of separation dictates the direction of the shear layer, which subsequently breaks down via Kelvin–Helmholtz instabilities. The wake then rolls up, advects downstream until it impinges on the second cylinder, and affects the subsequent shedding. The inflow turbulence level in the reference experiments is below 0.10%, so the

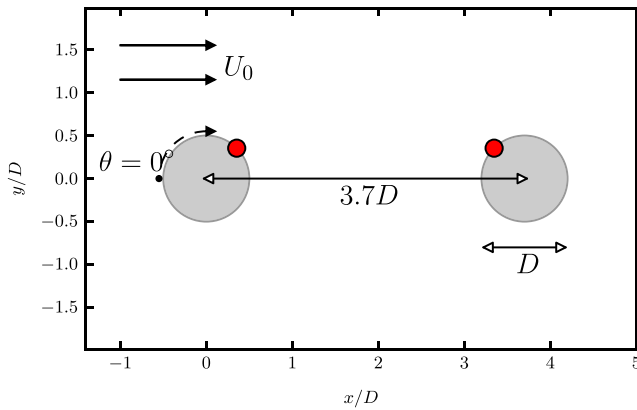


**Fig. 7** Side view of the tandem cylinder geometry. Red circles are points of surface pressure spectra calculations.

inlet quantities are prescribed as  $k_0 = 10^{-6}U_0^2$  and  $\omega_0 = 5U_0/D$  [73]. In the experiments, a fully turbulent shedding process is obtained by tripping the upstream and downstream cylinders. This allows for a fair comparison to hybrids that operate as RANS near the wall.

Because of the Mach number of  $M = 0.128$  (the experimental streamwise velocity was  $U_0 = 44$  m/s), compressibility effects are small and the incompressible formulation described in Sec. II.A is justified. The experimental database does, however, contain acoustic results from three microphones in the flow; see Table 2. Because density is held constant, the far-field noise contributions are found by using Curle's analogy [74] for sound generated by rigid bodies. The fluctuating sound pressure is reduced to surface integrals over both cylinders:

$$a_0^2(\rho - \rho_0) = -\frac{1}{4\pi a_0} \iint_{c_1+c_2} \frac{r_j n_j}{r^2} \partial_t p(\underline{y}, t - r/a_0) dS \quad (20)$$

where  $a_0$  and  $\rho_0$  are the reference speed of sound and density of the fluid at rest,  $n_i$  is the outward unit normal to the surface at point  $y_i$ ,  $x_i$  is the microphone position, and  $r_i$  is the difference  $r_i = x_i - y_i$  with  $r = |\underline{r}|$ .

The spanwise width suggested for hybrid simulations is  $3D$ , with periodic boundary conditions enforced, which is considerably smaller than the experimental values of  $12$ – $16D$ . Because of this disparity, when calculating the sound level at a point  $x_i$ , the acoustic data are corrected using the method of Kato et al. [75].

The two meshes used for hybrid calculations are denoted as base and CM for baseline and coarse meshes, respectively. The base mesh consists of 2 million cells, whereas the CM contains half this value. It should be noted that the base mesh is already very coarse; typically, hybrid simulations of the tandem cylinders are performed on much

finer grids [63]. Table 3 details specific mesh characteristics. To achieve the factor of two in the number of total cells  $N_{\text{cells}}$  and maintain the cylinder wall resolution ( $N_{\text{circum}}$  and  $\bar{y}_1^+$ ), the CM has been aggressively coarsened in the spanwise dimension  $N_{\text{span}}$ . Away from the cylinders, the plane  $N_{x-y}$  has also been coarsened significantly; particularly, there is a reasonable reduction in the number of cells along lines  $y = 0$  between the cylinders  $N_{\text{gap}}$ .

Statistics are gathered in the  $x$ – $y$  plane by averaging along the homogeneous  $z$  direction with time averaging of  $900U_0/D$  and  $400U_0/D$  time units for the base and CM cases, respectively. Surface pressure data are recorded around each cylinder at 20 spanwise locations consisting of 80 evenly spaced points in the  $x$ – $y$  plane. The sampling frequency resolution for surface pressure calculations during the base simulation is 83 kHz, with sample bin widths of 4 Hz collected. For the CM simulation, the sampling resolution is 17 kHz with sample bin widths of 2.7 Hz. For both cases, the values are within the levels dictated in the original study [63]. We did not gather time-resolved spectra for the DDES cases.

## 2. Results

Figures 8a and 8b are first-order statistics, with Figs. 8c and 8d showing the respective second-order quantities. Our hybrid framework for both mesh levels accurately depicts the first-order statistics, with equivalence between the two resolutions. Minor deviations are noticed between the base and CM, which grow from the initial recirculation zone and converge as the flow impinges on the second cylinder, and then finally become apparent once more in the downstream wake. There is an even higher correspondence between cases for the upstream and downstream surface pressures. In the DDES solutions, there is global inaccuracy because an incorrect flow state has been maintained. The cylinder spacing in the original experiment is close to the critical value between two flow regimes. Instead of realizing an asymmetric vortex-shedding pattern, the flow reattaches on the downstream cylinder, thus suppressing the correct periodic features on both meshes. Note that other hybrids have also incorrectly predicted this flow state [63]. Other studies have successfully predicted the flowfield by either drastically increasing the resolution, and thus the computational cost [63,76], or by altering the numerical scheme [67]. In the latter study, the DDES was shown to be sensitive to the scheme, whereas an FSM formulation was much more robust. Because of this global inaccuracy, the following comments pertain to our hybrid method only.

Second-order statistics are also well predicted, but they do show some disagreement. The two-dimensional turbulent kinetic energy  $k^{2d}$  (Fig. 8c) is overpredicted in the reverse flow region, stemming from extremely high near-wall values. By considering the pressure coefficient and its root-mean-square value at  $x = 0.5D$  (Fig. 8d), we can deduce that the flow within the recirculation bubble is too vigorous. The coarse mesh yields more dissipation than the baseline, dictated by  $N_{\text{gap}}$ . This reduces  $k$  to a more representative level, whereas the baseline peak value is too high. This is a good example of a cancellation of errors to yield a desirable result; production at the cylinder is too great, yet the subsequent dissipation is also.

The fluctuating pressure  $C_p'$  coefficient, plotted in Fig. 8d, provides information regarding the points of separation and wake impingement. On the upstream cylinder, the two maxima are the points of separation. The hybrid cases obtain their location correctly; however, there is a 20% overestimate in magnitude. This percentage is consistent across both the upstream and downstream cylinders. On the upstream cylinder, the implication is that the variance in the point of separation is much greater in the hybrids. The consistent overprediction may be due to long wavelength structures persisting in the RANS layer, which should break down to LES-like structures but cannot due to the strong effective filter. The outer peaks on the downstream cylinder are points of wake impingement: the locations of which are once again matched. Moving inward, the four peaks show the points of separation. There are four such separation points because, as upstream wakes impinge and pass around the cylinder, they force a similar alignment from the recirculation zone. As such, these peaks should be paired diagonally into two events: separation as a wake passes over the cylinder, and separation as a wake passes

**Table 2** Microphone locations

Microphone	$x$	$y$
1	$-8.33D$	$27.82D$
2	$9.11D$	$32.49D$
3	$26.55D$	$27.82D$

**Table 3** Mesh properties used for hybrid tandem cylinder prediction<sup>a</sup>

	$N_{\text{cells}}$	$N_{\text{span}}$	$N_{\text{gap}}$	$N_{x-y}$	$N_{\text{circum}}^u$	$\bar{y}_1^{+,u}$	$N_{\text{circum}}^d$	$\bar{y}_1^{+,d}$
Base	2.1 mio	40	154	53,000	173	0.64	186	0.73
CM	0.97 mio	26	123	38,000	173	0.68	186	0.77

<sup>a</sup> $u$  and  $d$  superscripts denote upstream and downstream cylinders.



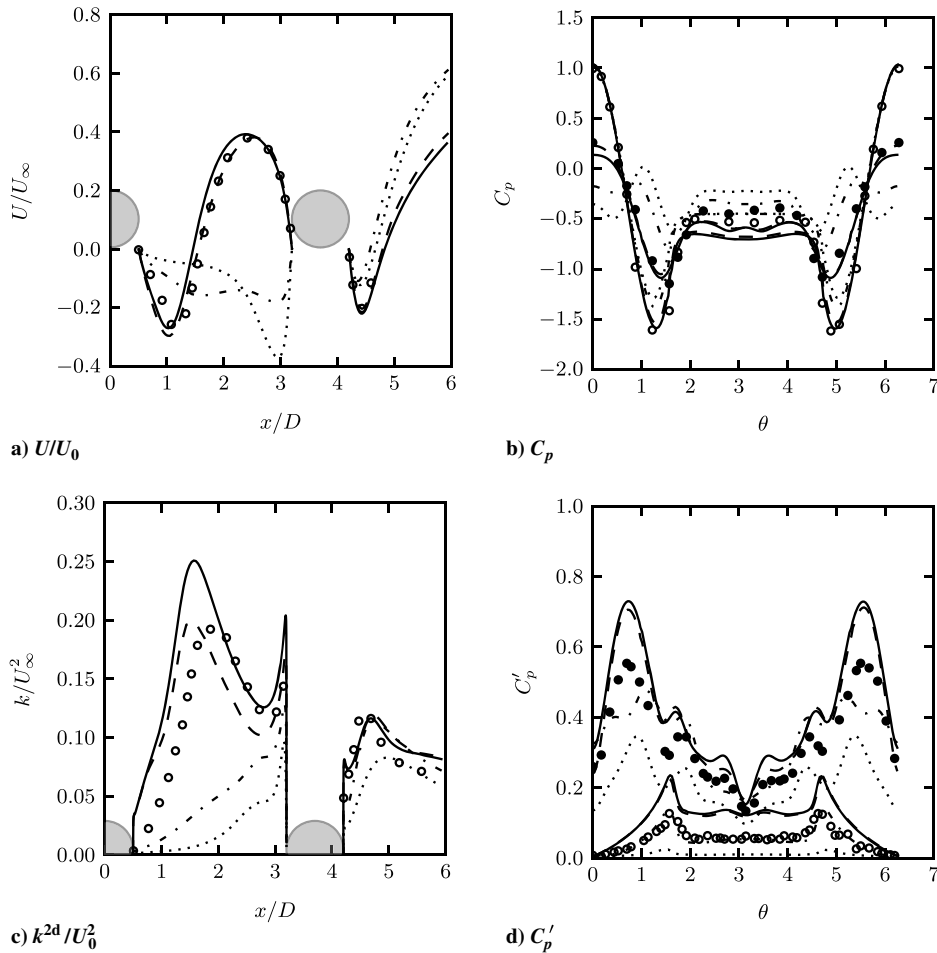


**Fig. 8** Tandem cylinder flow statistics. (o) Experimental values; (—) base; (---) CM; (-.-) base-DDES; (...) CM-DDES (open circles: upstream cylinder; filled circles: downstream cylinder).

under. The points of separation closest to the impinged wake show this occurs too early, demanding a corresponding shift from the inner most peaks, so we can deduce that the recirculation zone moves slightly too far. The innermost peaks, especially for the base profile, are high. This suggests that there are too many turbulent structures “leaking” around the other side of the cylinder as a wake passes over.

Figures 9a and 9b are plots of the power spectral density  $P_p$  at the two locations highlighted in Fig. 7. Both resolutions predict identical Strouhal numbers and the presence of the single pronounced harmonic peak. Beyond approximately  $f = 1000$  Hz, the spectral content diminishes in the hybrid cases: more so for the CM. This hints

at the influence of the effective filter on even moderately large scales resolved in the flow, and we can identify the effect of coarsening the grid on the higher frequencies.

The majority of the acoustic content is a consequence of the downstream cylinder. Because of the excellent agreement in Fig. 9b, the acoustic field has been extremely well predicted at all three microphone locations. This is shown in Figs. 10a–10c. The shape of the spectrum is highly representative for both hybrid cases, even at high frequencies. The slope of the power spectral density, especially for the baseline case, is indicative of the experimental result up to the point of the sampling frequency.

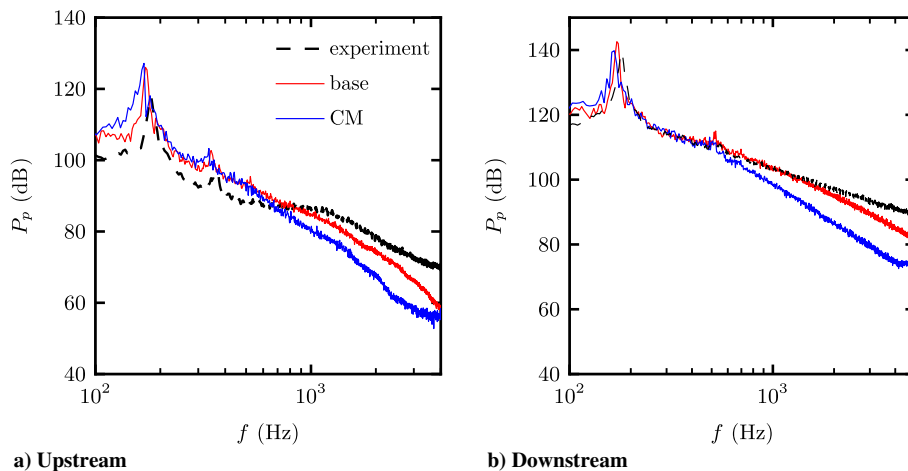


**Fig. 9** Power spectral densities at the two locations denoted in Fig. 7.

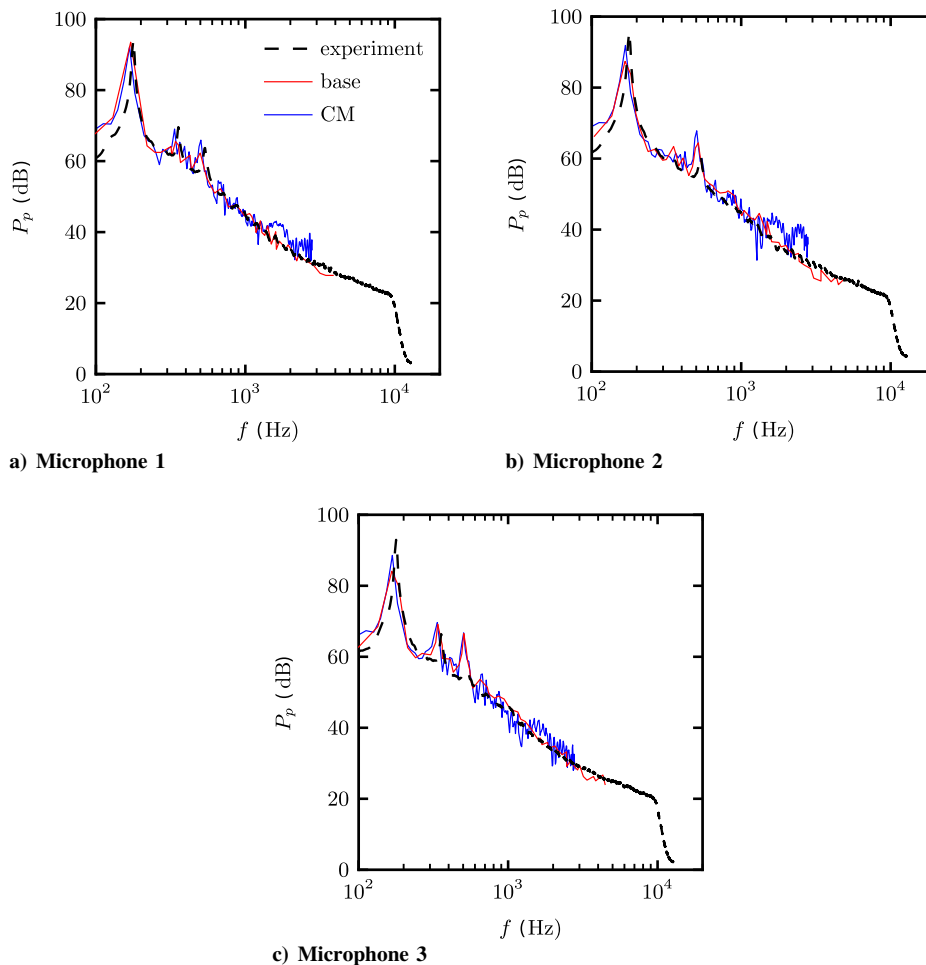


Fig. 10 Acoustic predictions at the microphone locations in Table 2.

By aggregating all the results collected from this case, we can conclude that the hybrid methodology has performed admirably on both mesh resolutions. The simulations conducted here are on grids coarser than typical for this case (by up to an order of magnitude) [63]. The CM simulation, which is the cheapest currently known to the authors, has especially produced excellent results at a fraction of the cost. This economical use of grid points has not sacrificed computational accuracy; the workshop [63] conducted using this test case has provided a wealth of comparison to other hybrids, which shows our method is extremely competitive.

#### IV. Conclusions

The novel hybrid RANS/LES approach, derived using a data-driven method, has shown consistent predictions for three different flow types: homogeneous isotropic turbulence (Sec. II.E), periodic hills, and the tandem cylinder test cases. This consistency was across two mesh levels, with each coarse-mesh simulation considered a very large-eddy simulation. The agreement to the reference data and comparison against an existing approach for a varied set of quantities were excellent.

These pleasing results (especially with respect to mesh independence) were obtained using a novel convection scheme  $\psi$  that was built considering the new damping function, resulting in a direct mapping of a model regime to an appropriate numerical blending. Furthermore, the  $g$  function assisted with only activating the model in vortical flow. As a consequence, the numerics and model were well married.

The hybrid methodology has been coupled to an explicit algebraic stress model; this was for the performance near the Reynolds-averaged Navier–Stokes (RANS) limit. Caring for the regime of

$f \rightarrow 1$  was deemed the most robust; errors in this limit were amplified with respect to errors in modeling as  $f \rightarrow 0$ . The influence of the RANS closure on the small scales should be investigated; a priori studies will be helpful for this issue.

The function  $f$  was built using direct numerical simulation (DNS) data from a pipe; the dependence on these data should be explored. This method could be improved by simultaneously considering more datasets that included complex flow structures with differing-order filters so that a contribution function suitable for a wide range of flow problems could be found. This could be extended further to vary the filter kernel in order to explore the implicit functional dependence of  $f$  on such a process. Whilst the optimization of the damping function is computationally inexpensive, the validation of the model is. Consequently, only two cases have been presented in Sec. III. This cost-effective model building implies that the training data can be very large, consisting of hundreds of thousands of data points from many different flowfields at differing filter levels. Of particular interest would be time filtering of DNS data to explore the unsteady RANS limit of the unified hybrid RANS/LES.

Finally, another avenue of exploration would be to build specialized contribution functions that could be generated for problems that contained a dominant feature such as transition or massively separated, periodic flow.

#### Appendix: Full Model Transport Equations

This Appendix closes the hybrid RANS/LES model detailed in Sec. II: particularly, the underlying RANS model. The Reynolds stress is defined by Eq. (4). The extra anisotropy is found from the following:

$$a_{ij}^x = \beta_2 \tau^2 \left( \tilde{S}_{ik} \tilde{S}_{kj} - \frac{1}{3} \tilde{S}_{mn} \tilde{S}_{nm} \delta_{ij} \right) + \beta_4 \tau^2 \left( \tilde{S}_{ik} \tilde{\Omega}_{kj} - \tilde{\Omega}_{ik} \tilde{S}_{kj} \right) \quad (\text{A1})$$

where  $\Omega_{ij}$  is the rotation rate tensor, and  $\tau = (1/\beta^* \omega)$  is the turbulent timescale. The coefficients  $\beta$  and the specific dissipation rate  $\omega$  will be defined in the following. The subgrid viscosity required for Eq. (4) is defined as follows:

$$\nu_{\text{sgs}} = -\frac{1}{2} f \beta_1 k \tau \quad (\text{A2})$$

The dissipation rate  $\varepsilon$  is evaluated from

$$\varepsilon = \frac{k^{3/2}}{f \ell^{\text{rans}}} \quad (\text{A3})$$

where the characteristic length scale is  $\ell^{\text{rans}} = k^{1/2}/\beta^* \omega$ .

The coefficients  $\beta$  are, respectively,

$$\beta^* = 0.09, \quad \beta_1 = -A_1 N/Q, \quad \beta_2 = 2A_1 A_2/Q, \quad \beta_4 = -A_1/Q \quad (\text{A4})$$

The constants  $A$  are

$$A_1 = 1.22, \quad A_2 = 0.47, \quad A_3 = 0.88, \quad A_4 = 2.37 \quad (\text{A5})$$

$Q$  is found from

$$Q = N^2 - 2\tau^2 \tilde{\Omega}_{mn} \tilde{\Omega}_{nm} - \frac{2}{3} \tau^2 A_2^2 \tilde{S}_{mn} \tilde{S}_{nm} \quad (\text{A6})$$

where  $N$  is

$$N = \begin{cases} \frac{A_3}{3} + (P_1 + \sqrt{P_2})^{1/3} + (P_1 - \sqrt{P_2})^{1/3}, & P_2 \geq 0 \\ \frac{A_3}{3} + 2(P_1^2 - P_2)^{1/6} \cos \left[ \frac{1}{3} \arccos(P_1(P_1^2 - P_2)^{-1/2}) \right], & P_2 < 0 \end{cases} \quad (\text{A7})$$

and the  $P$

$$P_1 = \left[ \frac{A_3^2}{27} + \left( \frac{A_1 A_4}{6} - \frac{2}{9} A_2^2 \right) \tau^2 \tilde{S}_{mn} \tilde{S}_{nm} - \frac{2}{3} \tau^2 \tilde{\Omega}_{mn} \tilde{\Omega}_{nm} \right] A_3 \quad (\text{A8})$$

$$P_2 = P_1^2 - \left[ \frac{A_3^2}{9} + \left( \frac{A_1 A_4}{6} + \frac{2}{9} A_2^2 \right) \tau^2 \tilde{S}_{mn} \tilde{S}_{nm} + \frac{2}{3} \tau^2 \tilde{\Omega}_{mn} \tilde{\Omega}_{nm} \right]^3 \quad (\text{A9})$$

The relations for  $N$ ,  $P$ , and  $Q$  are the result of assuming the anisotropy tensor is a function of  $S_{ij}$ ,  $\Omega_{ij}$ , and  $P_k/\varepsilon$ .  $P_k = -\tau_{ij}^{\text{hyb}} \partial_{x_j} \tilde{u}_i$  is the production of turbulent kinetic energy.

Finally, to close the equation set, transport equations for  $k$  and  $\omega$  are required. We use the form of the Menter shear-stress transport [23] model, modified by Hellsten [77]:

$$\partial_t k + \tilde{u}_j \partial_{x_j} k = P_k - \varepsilon + \partial_{x_j} [(\nu + \sigma_k \nu_{\text{sgs}}) \partial_{x_j} k] \quad (\text{A10})$$

$$\partial_t \omega + \tilde{u}_j \partial_{x_j} \omega = \gamma \frac{\omega}{k} P_k - \zeta \omega^2 + \partial_{x_j} [(\nu + \sigma_\omega \nu_{\text{sgs}}) \partial_{x_j} \omega] + \sigma_d CD_{k\omega}^+ \quad (\text{A11})$$

Left to be defined are the following:

$$\begin{aligned} CD_{k\omega} &= \partial_{x_j} k \partial_{x_j} \omega, & CD_{k\omega}^+ &= \max[CD_{k\omega}, 0], \\ \psi &= \psi_2 + f_b(\psi_1 - \psi_2), & f_b &= \tanh(1.5\Gamma^4) \\ \Gamma &= \min \left[ \max \left[ \frac{k^{1/2}}{\beta^* \omega y}, \frac{500\nu}{y^2 \omega} \right], \varphi \right], & \varphi &= \frac{20k}{\max \left[ y^2 CD_{k\omega}, 200k_\infty \right]} \end{aligned} \quad (\text{A12})$$

where  $\psi$  is a coefficient from Eqs. (30) and (31) that has two definitions, defined by a subscript of 1 or 2. Each  $\psi$  is blended between two values,  $\psi_1$  and  $\psi_2$ , such that  $\psi_1$  is active near the wall and  $\psi_2$  far from it. These coefficients, along with  $\sigma_k$ , are given as follows:

$$\begin{aligned} \sigma_{\omega 1} &= 0.53, & \sigma_{\omega 2} &= 1.00, & \sigma_{d1} &= 1.0, & \sigma_d &= 0.4, & \sigma_k &= 1.1, \\ \gamma_1 &= 0.518, & \gamma_2 &= 0.44, & \zeta_1 &= 0.0747, & \zeta_2 &= 0.0828 \end{aligned} \quad (\text{A13})$$

## Acknowledgments

This work was funded in part by the victorian endowment for science, knowledge and innovation and an *Engineering and Physical Sciences Research Council* Doctoral Training Centre grant (EP/G03690X/1).

## References

- [1] Aljure, D., Lehmkuhl, O., Rodriguez, I., and Oliva, A., "Flow and Turbulent Structures Around Simplified Car Models," *Computers and Fluids*, Vol. 96, 2014, pp. 122–135. doi:10.1016/j.compfluid.2014.03.013
- [2] Hosseini, S. M., Vinuesa, R., Schlatter, P., Hanifi, A., and Henningson, D. S., "Direct Numerical Simulation of the Flow Around a Wing Section at Moderate Reynolds Number," *International Journal of Heat and Fluid Flow*, Vol. 61, 2016, pp. 117–128. doi:10.1016/j.ijheatfluidflow.2016.02.001
- [3] Michelassi, V., Chen, L.-W., Pichler, R., and Sandberg, R. D., "Compressible Direct Numerical Simulation of Low-Pressure Turbines, Part II: Effect of Inflow Disturbances," *Journal of Turbomachinery*, Vol. 137, No. 7, 2015, Paper 071005. doi:10.1115/1.4029126
- [4] Moser, R., Kim, J., and Mansour, N. N., "Direct Numerical Simulation of Turbulent Channel Flow up to  $Re_\tau = 590$ ," *Physics of Fluids*, Vol. 11, No. 4, 1999, pp. 943–945. doi:10.1063/1.869966
- [5] Kaneda, Y., Ishihara, T., Yokokawa, M., Itakura, K., and Uno, A., "Energy Dissipation Rate and Energy Spectrum in High Resolution Direct Numerical Simulations of Turbulence in a Periodic Box," *Physics of Fluids*, Vol. 15, No. 2, 2003, p. L21. doi:10.1063/1.1539855
- [6] Lee, M., and Moser, R. D., "Direct Numerical Simulation of Turbulent Channel Flow up to  $Re_\tau \approx 5200$ ," *Journal of Fluid Mechanics*, Vol. 774, 2015, pp. 395–415. doi:10.1017/jfm.2015.268
- [7] Sagaut, P., *Large Eddy Simulation for Incompressible Flows: An Introduction*, Springer Science and Business Media, New York, 2006, p. 558.
- [8] Chapman, D. K., "Computational Aerodynamics Development and Outlook," *AIAA Journal*, Vol. 17, No. 12, 1979, pp. 1293–1313. doi:10.2514/3.61311
- [9] Choi, H., and Moin, P., "Grid-Point Requirements for Large Eddy Simulation: Chapman's Estimates Revisited," *Physics of Fluids (1994–Present)*, Vol. 24, No. 1, 2012, Paper 011702.
- [10] Pope, S., *Turbulent Flows*, Cambridge Univ. Press, Cambridge, U.K., 2000, p. 802.
- [11] Fröhlich, J., and von Terzi, D., "Hybrid LES/RANS Methods for the Simulation of Turbulent Flows," *Progress in Aerospace Sciences*, Vol. 44, No. 5, 2008, pp. 349–377. doi:10.1016/j.paerosci.2008.05.001
- [12] Wilcox, D. C., *Turbulence Modeling for CFD*, 2nd ed., DCW Industries, La Cañada, CA, 1998, p. 460.
- [13] Leschziner, M., *Statistical Turbulence Modelling for Fluid Dynamics—Demystified: An Introductory Text for Graduate Engineering Students*, World Scientific, Singapore, 2015, p. 407.

- [14] Jakirlić, S., Jester-Zürker, R., and Tropea, C., "Report on the 9th ERCOFTAC/IAHR/COST Workshop on Refined Turbulence Modeling," *ERCOFTAC Bulletin*, Vol. 55, 2001.
- [15] Schneider, H., von Terzi, D., Bauer, H.-J., and Rodi, W., "Reliable and Accurate Prediction of Three-Dimensional Separation in Asymmetric Diffusers Using Large-Eddy Simulation," *Journal of Fluids Engineering*, Vol. 132, No. 3, 2010, Paper 031101.
- [16] Pope, S. B., "A Perspective on Turbulence Modeling," *Modeling Complex Turbulent Flows*, Springer, New York, 1999, pp. 53–67.
- [17] Spalart, P. R., Jou, W.-H., Strelets, M., and Allmaras, S. R., "Comments on the Feasibility of LES for Wings, and on a Hybrid RANS/LES Approach," *Advances in DNS/LES*, edited by C. Liu, and Z. Liu, Greyden Press, Dayton, OH, 1997, pp. 137–147.
- [18] Speziale, C. G., "Computing Non-Equilibrium Turbulent Flows with Time-Dependent RANS and VLES," *15th International Conference on Numerical Methods in Fluid Dynamics*, Springer, New York, 1997, pp. 123–129.
- [19] Fadaei-Ghotbi, A., Friess, C., Manceau, R., Gatski, T. B., and Borée, J., "Temporal Filtering: A Consistent Formalism for Seamless Hybrid RANS–LES Modeling in Inhomogeneous Turbulence," *International Journal of Heat and Fluid Flow*, Vol. 31, No. 3, 2010, pp. 378–389. doi:10.1016/j.ijheatfluidflow.2009.12.008
- [20] Chaouat, B., and Schiestel, R., "A New Partially Integrated Transport Model for Subgrid-Scale Stresses and Dissipation Rate for Turbulent Developing Flows," *Physics of Fluids (1994–Present)*, Vol. 17, No. 6, 2005, Paper 065106.
- [21] Germano, M., "Properties of the Hybrid RANS/LES Filter," *Theoretical and Computational Fluid Dynamics*, Vol. 17, No. 4, 2004, pp. 225–231. doi:10.1007/s00162-004-0116-6
- [22] Chien, K.-Y., "Predictions of Channel and Boundary-Layer Flows with a Low-Reynolds-Number Turbulence Model," *AIAA Journal*, Vol. 20, No. 1, 1982, pp. 33–38. doi:10.2514/3.51043
- [23] Menter, F. R., "Two-Equation Eddy-Viscosity Turbulence Models for Engineering Applications," *AIAA Journal*, Vol. 32, No. 8, 1994, pp. 1598–1605. doi:10.2514/3.12149
- [24] Wilcox, D. C., "Formulation of the k- $\omega$  Turbulence Model Revisited," *AIAA Journal*, Vol. 46, No. 11, 2008, pp. 2823–2838. doi:10.2514/1.36541
- [25] Smagorinsky, J., "General Circulation Experiments with the Primitive Equations," *Monthly Weather Review*, Vol. 91, No. 3, 1963, pp. 99–164. doi:10.1175/1520-0493(1963)091<0099:GCEWTP>2.3.CO;2
- [26] Piomelli, U., and Balaras, E., "Wall-Layer Models for Large-Eddy Simulations," *Annual Review of Fluid Mechanics*, Vol. 34, No. 1, 2002, pp. 349–374. doi:10.1146/annurev.fluid.34.082901.144919
- [27] Sagaut, P., Deck, S., and Terracol, M., *Multiscale and Multiresolution Approaches in Turbulence: LES, DES and Hybrid RANS/LES Methods: Applications and Guidelines*, World Scientific, Singapore, 2013, p. 425.
- [28] Schumann, U., "Subgrid Scale Model for Finite Difference Simulations of Turbulent Flows in Plane Channels and Annuli," *Journal of Computational Physics*, Vol. 18, No. 4, 1975, pp. 376–404. doi:10.1016/0021-9991(75)90093-5
- [29] Deardorff, J. W., "A Numerical Study of Three-Dimensional Turbulent Channel Flow at Large Reynolds Numbers," *Journal of Fluid Mechanics*, Vol. 41, No. 2, 1970, pp. 453–480. doi:10.1017/S0022112070000691
- [30] Balaras, E., and Benocci, C., "Subgrid-Scale Models in Finite-Difference Simulations of Complex Wall Bounded Flows," *AGARD Conference Proceedings, 74th Fluid Dynamics Symposium*, 551, Chania, Crete, Greece, April 1994.
- [31] Quémeré, P., and Sagaut, P., "Zonal Multi-Domain RANS/LES Simulations of Turbulent Flows," *International Journal for Numerical Methods in Fluids*, Vol. 40, No. 7, 2002, pp. 903–925. doi:10.1002/fld.v40:7
- [32] Tucker, P. G., and Davidson, L., "Zonal k- $\omega$  Based Large Eddy Simulations," *Computers and Fluids*, Vol. 33, No. 2, 2004, pp. 267–287. doi:10.1016/S0045-7930(03)00039-2
- [33] Schlüter, J., Pitsch, H., and Moin, P., "Large-Eddy Simulation Inflow Conditions for Coupling with Reynolds-Averaged Flow Solvers," *AIAA Journal*, Vol. 42, No. 3, 2004, pp. 478–484. doi:10.2514/1.3488
- [34] Deck, S., "Zonal-Detached-Eddy Simulation of the Flow Around a High-Lift Configuration," *AIAA Journal*, Vol. 43, No. 11, 2005, pp. 2372–2384. doi:10.2514/1.16810
- [35] Batten, P., Goldberg, U., and Chakravarthy, S., "LNS—An Approach Towards Embedded LES," *AIAA Paper 2002-0427*, 2002.
- [36] Chaouat, B., and Schiestel, R., "Hybrid RANS/LES Simulations of the Turbulent Flow over Periodic Hills at High Reynolds Number Using the PITM Method," *Computers and Fluids*, Vol. 84, Sept. 2013, pp. 279–300. doi:10.1016/j.compfluid.2013.06.012
- [37] Girimaji, S. S., "Partially-Averaged Navier–Stokes Model for Turbulence: A Reynolds-Averaged Navier–Stokes to Direct Numerical Simulation Bridging Method," *Journal of Applied Mechanics*, Vol. 73, No. 3, 2006, pp. 413–421. doi:10.1115/1.2151207
- [38] Rodi, W., Mansour, N. N., and Michelassi, V., "One-Equation Near-Wall Turbulence Modeling with the Aid of Direct Simulation Data," *Journal of Fluids Engineering*, Vol. 115, No. 2, 1993, pp. 196–205. doi:10.1115/1.2910124
- [39] Breuer, M., Jaffrézic, B., and Arora, K., "Hybrid LES–RANS Technique Based on a One-Equation Near-Wall Model," *Theoretical and Computational Fluid Dynamics*, Vol. 22, Nos. 3–4, 2008, pp. 157–187. doi:10.1007/s00162-007-0067-9
- [40] Menter, F. R., Kuntz, M., and Bender, R., "A Scale-Adaptive Simulation Model for Turbulent Flow Predictions," *41st Aerospace Sciences Meeting and Exhibit*, AIAA Paper 2003-0767, 2003.
- [41] Travin, A., Shur, M., Spalart, P. R., and Strelets, M., "On URANS Solutions with LES-Like Behaviour," *Congress on Computational Methods in Applied Sciences and Engineering, ECCOMAS*, edited by P. Neittaanmäki, T. Rossi, K. Majava, and O. Pironnea, 2004.
- [42] Spalart, P. R., Deck, S., Shur, M., Squires, K., Strelets, M. K., and Travin, A., "A New Version of Detached-Eddy Simulation, Resistant to Ambiguous Grid Densities," *Theoretical and Computational Fluid Dynamics*, Vol. 20, No. 3, 2006, pp. 181–195. doi:10.1007/s00162-006-0015-0
- [43] Baggett, J. S., "On the Feasibility of Merging LES with RANS for the Near-Wall Region of Attached Turbulent Flows," *Annual Research Briefs*, Center for Turbulence Research Annual Research Briefs, 1998, pp. 267–277.
- [44] Nikitin, N., Nicoud, F., Wasistho, B., Squires, K., and Spalart, P., "An Approach to Wall Modeling in Large-Eddy Simulations," *Physics of Fluids (1994–Present)*, Vol. 12, No. 7, 2000, pp. 1629–1632. doi:10.1063/1.870414
- [45] Weatheritt, J., Sandberg, R., and Lozano-Durán, A., "Reynolds Stress Structures in the Hybrid RANS/LES of a Planar Channel," *Journal of Physics: Conference Series*, Vol. 708, No. 1, 2016, Paper 012008.
- [46] Menter, F., and Kuntz, M., "Adaptation of Eddy-Viscosity Turbulence Models to Unsteady Separated Flow Behind Vehicles," *The Aerodynamics of Heavy Vehicles: Trucks, Buses, and Trains*, Springer, New York, 2004, pp. 339–352.
- [47] Shur, M. L., Spalart, P. R., Strelets, M. K., and Travin, A. K., "A Hybrid RANS–LES Approach with Delayed-DES and Wall-Modelled LES Capabilities," *International Journal of Heat and Fluid Flow*, Vol. 29, No. 6, 2008, pp. 1638–1649. doi:10.1016/j.ijheatfluidflow.2008.07.001
- [48] Gopalan, H., Heinz, S., and Stöllinger, M. K., "A Unified RANS–LES Model: Computational Development, Accuracy and Cost," *Journal of Computational Physics*, Vol. 249, 2013, pp. 249–274. doi:10.1016/j.jcp.2013.03.066
- [49] Ferreira, C., "Gene Expression Programming: A New Adaptive Algorithm for Solving Problems," *Complex Systems*, Vol. 13, No. 2, 2001, pp. 87–129.
- [50] Fasel, H. F., Von Terzi, D. A., and Sandberg, R. D., "A Methodology for Simulating Compressible Turbulent Flows," *Journal of Applied Mechanics*, Vol. 73, No. 3, 2006, pp. 405–412. doi:10.1115/1.2150231
- [51] Weinmann, M., Sandberg, R. D., and Doolan, C., "Tandem Cylinder Flow and Noise Predictions Using a Hybrid RANS/LES Approach," *International Journal of Heat and Fluid Flow*, Vol. 50, 2014, pp. 263–278. doi:10.1016/j.ijheatfluidflow.2014.08.011
- [52] Pope, S. B., "A More General Effective-Viscosity Hypothesis," *Journal of Fluid Mechanics*, Vol. 72, No. 2, 1975, pp. 331–340. doi:10.1017/S0022112075003382
- [53] Speziale, C. G., Sarkar, S., and Gatski, T. B., "Modelling the Pressure-Strain Correlation of Turbulence: An Invariant Dynamical Systems Approach," *Journal of Fluid Mechanics*, Vol. 227, June 1991, pp. 245–272. doi:10.1017/S0022112091000101
- [54] Meyers, J., and Sagaut, P., "On the Model Coefficients for the Standard and the Variational Multi-Scale Smagorinsky Model," *Journal of Fluid Mechanics*, Vol. 569, 2006, pp. 287–319. doi:10.1017/S0022112006002850
- [55] Sandberg, R. D., "Numerical Investigation of Transitional and Turbulent Supersonic Axisymmetric Wakes," Ph.D. Thesis, The Univ. of Arizona, Tucson, AZ, 2004.

- [56] Germano, M., "Comment on 'Turbulence Modeling for Time-Dependent RANS and VLES: A Review'," *AIAA Journal*, Vol. 36, No. 9, 1998, p. 1766.  
doi:10.2514/3.14045
- [57] Ferreira, C., "Function Finding and the Creation of Numerical Constants in Gene Expression Programming," *Proceedings of the 7th Online World Conference on Soft Computing in Industrial Applications*, edited by J. M. Benitez, O. Cordón, F. Hoffman, and R. Roy, Springer, London, 2003, pp. 257–265.  
doi:10.1007/978-1-4471-3744-3\_25
- [58] Wallin, S., and Johansen, A. V., "An Explicit Algebraic Reynolds Stress Model for Incompressible and Compressible Turbulent Flows," *Journal of Fluid Mechanics*, Vol. 403, 2000, pp. 89–132.  
doi:10.1017/S0022112099007004
- [59] Travin, A., Shur, M., Strelets, M., and Spalart, P., "Physical and Numerical Upgrades in the Detached-Eddy Simulation of Complex Turbulent Flows," *Advances in LES of Complex Flows*, Springer, New York, 2002, pp. 239–254.
- [60] Davidson, L., and Peng, S.-H., "Hybrid LES-RANS Modelling: A One-Equation SGS Model Combined with  $k - \omega$  a Model for Predicting Recirculating Flows," *International Journal for Numerical Methods in Fluids*, Vol. 43, No. 9, 2003, pp. 1003–1018.  
doi:10.1002/(ISSN)1097-0363
- [61] Mathey, F., Cokljat, D., Bertoglio, J.-P., and Sergent, E., "Specification of LES Inlet Boundary Condition Using Vortex Method," *Progress in Computational Fluid Dynamics*, Vol. 6, Nos. 1–3, 2006, pp. 58–67.  
doi:10.1504/PCFD.2006.009483
- [62] Šarić, S., Jakirlić, S., Breuer, M., Jaffrézic, B., Deng, G., Chikhaoui, O., Fröhlich, J., Von Terzi, D., Manhart, M., and Peller, N., "Evaluation of Detached Eddy Simulations for Predicting the Flow Over Periodic Hills," *ESAIM: Proceedings*, Vol. 16, EDP Sciences, Les Ulis, France, 2007, pp. 133–145.  
doi:10.1051/proc:2007016
- [63] Lockard, D. P., "Summary of the Tandem Cylinder Solutions from the Benchmark Problems for Airframe Noise Computations-I Workshop," AIAA Paper 2011-353, 2011.
- [64] Uzun, A., and Hussaini, M. Y., "An Application of Delayed Detached Eddy Simulation to Tandem Cylinder Flow Field Prediction," *Computers and Fluids*, Vol. 60, 2012, pp. 71–85.  
doi:10.1016/j.compfluid.2012.02.029
- [65] Gopalan, H., and Jaiman, R., "Numerical Study of the Flow Interference Between Tandem Cylinders Employing Non-Linear Hybrid URANS–LES Methods," *Journal of Wind Engineering and Industrial Aerodynamics*, Vol. 142, 2015, pp. 111–129.  
doi:10.1016/j.jweia.2015.03.017
- [66] Temmerman, L., and Leschziner, M. A., "Large Eddy Simulation of Separated Flow in a Streamwise Periodic Channel Constriction," *TSFP Digital Library Online*, Begel House Inc., 2001.
- [67] Weatheritt, J., "The Development of Data Driven Approaches to Further Turbulence Closures," Ph.D. Thesis, Univ. of Southampton, Southampton, England, U.K., 2015.
- [68] Jenkins, L. N., Khorrami, M. R., Choudhari, M. M., and McGinley, C. B., "Characterization of Unsteady Flow Structures Around Tandem Cylinders for Component Interaction Studies in Airframe Noise," AIAA Paper 2005-2812, 2005.
- [69] Jenkins, L. N., Neuhart, D. H., McGinley, C. B., Choudhari, M. M., and Khorrami, M. R., "Measurements of Unsteady Wake Interference Between Tandem Cylinders," AIAA Paper 2006-3202, 2006.
- [70] Lockard, D. P., Khorrami, M. R., Choudhari, M. M., Hutcheson, F. V., Brooks, T. F., and Stead, D. J., "Tandem Cylinder Noise Predictions," AIAA Paper 2007-3450, 2007.
- [71] Khorrami, M. R., Choudhari, M. M., Lockard, D. P., Jenkins, L. N., and McGinley, C. B., "Unsteady Flowfield Around Tandem Cylinders as Prototype Component Interaction in Airframe Noise," *AIAA Journal*, Vol. 45, No. 8, 2007, pp. 1930–1941.  
doi:10.2514/1.23690
- [72] Neuhart, D. H., Jenkins, L. N., Choudhari, M. M., and Khorrami, M. R., "Measurements of the Flowfield Interaction Between Tandem Cylinders," AIAA Paper 2009-3275, 2009.
- [73] Spalart, P. R., and Rumsey, C. L., "Effective Inflow Conditions for Turbulence Models in Aerodynamic Calculations," *AIAA Journal*, Vol. 45, No. 10, 2007, pp. 2544–2553.  
doi:10.2514/1.29373
- [74] Curle, N., "The Influence of Solid Boundaries Upon Aerodynamic Sound," *Proceedings of the Royal Society of London, Series A: Mathematical, Physical and Engineering Sciences*, Vol. 231, No. 1187, 1955, pp. 505–514.
- [75] Kato, C., Iida, A., Takano, Y., Fujita, H., and Ikegawa, M., "Numerical Prediction of Aerodynamic Noise Radiated from Low Mach Number Turbulent Wake," *31st AIAA Aerospace Sciences Meeting and Exhibit*, AIAA Paper 1993-0145, 1993.
- [76] Schwamborn, D., Probst, A., Kessler, R., Valentino, M., and Weinman, K., "Turbulence Resolving Simulations of the Flow About a Tandem Cylinder and a Rudimentary Landing Gear," *Notes on Numerical Fluid Mechanics and Multidisciplinary Design*, Springer, New York, 2012, pp. 59–75.
- [77] Hellsten, A. K., "New Advanced  $k - \omega$  Turbulence Model for High-Lift Aerodynamics," *AIAA Journal*, Vol. 43, No. 9, 2005, pp. 1857–1869.  
doi:10.2514/1.13754

C. Wen  
Associate Editor